IEEE Access
Multidisciplinary | Rapid Review | Open Access Journal

SPECIAL SECTION ON DEEP LEARNING ALGORITHMS FOR INTERNET OF MEDICAL THINGS

Received March 23, 2020, accepted April 24, 2020, date of publication May 11, 2020, date of current version May 26, 2020.

Digital Object Identifier 10.1109/ACCESS.2020.2993872

Design of Automatic Lung Nodule Detection System Based on Multi-Scene Deep Learning Framework

QINGHAI ZHANG AND XIAOJING KONG
Imaging Department, The Third People's Hospital of Zibo, Zibo 255000, China
Corresponding author: Xiaojing Kong (kxj0827@163.com)

ABSTRACT Nowadays, the efficient identification of the lung nodule greatly leads to the chance of lung cancer risk assessment. Hence, the exact locations of lung nodules are a critical and complicated task. Researchers in this area have been working widely for almost two years. However, previous computer-aided detection (CAD) modules, such as transforming CT, segmenting the lung nodule and extracting the features are mostly complex and time-consuming, because more modules will require the creation of a complete image processing system. In addition, certain state-of-the-art deep learning systems are specified in the database standard. For this purpose, this paper suggests an efficient identification system for lung nodules based on Multi-Scene Deep Learning Framework (MSDLF) by the vesselness filter. A four-channel CNN model is designed to enhance the radiologist's knowledge in the detection of four-stage nodules by integrating two image Scenes. This model can be applied in two different classes. The results show that the Multi-Scene Deep Learning Framework (MSDLF) is efficient for increasing the accuracy and significantly reducing false positives in an enormous amount of image data in the detection of lung nodules.

INDEX TERMS Multi-scene deep learning framework, vesselness filter, convolutional neural network (CNN), lung nodules.

I. INTRODUCTION

Lung cancer is one of the world's most dangerous cancers. However, the early detection significantly increases the survival rate of lung cancer [1]. The cells in the lung have small growths of cancer (malignant) and non-cancerous (benign) lung nodules [2], [3]. For essential prognosis, the early diagnosis of malignant lung nodules is important. Cancer lung nodules in the early stage are very similar to non-cancer nodules and need to be differentially identified based on small morphological variations, positions, and medical biomarkers [4]. The difficult task is for the early lung nodules to calculate the risk of malignancy. A computer tomography scan (CT) (morphological evaluation), Positron Emissions Tomography (PET), and needle prick biopsy exam is used in many diagnostic procedures [5] in connection with early diagnosis of malignant lung nodules in clinical settings [6], [7]. Moreover, medical practitioners are primarily using invasive approaches such as biopsies or operations for differentiating benign from malignant lung nodules [8]. Invasive methods involve many risks and raise the anxiety of patients for such a delicate and sensitive organ [9].

Computing tomography (CT) imaging is the best approach for analyzing lung diseases [10]. In addition, the incidence of CT scans with false positive in cancer radiation results is substantially less than the normal CT dose, due to the low dosage of CT [11]. Results show no significant differences in detection sensitivities between low and normal CT images. In the majority of the population identified with low dose CT scans relative to the Chest X-rays the national lung screening tests (NLST) for deaths from cancer have significantly reduced [12]. Advanced clinical information (thinner slices) and advanced imaging techniques improve the identification sensitivity of lung nodules [13], [14]. Moreover, this significantly increases the datasets. In one scan up to 500 sections/slices are generated according to the thickness of the slice. It takes 2-3, 5 minutes for a trained radiologist to test a single slice [15]. A radiologist's workload increases significantly in order to detect the potential presence of a nodule [16], [17].

Results show only a 68% accurate diagnosis of lung nodules when only a single X-ray specialist conducts the analysis

The associate editor coordinating the review of this manuscript and approving it for publication was Wei Wei.

and with both radiologists up to 82% of the time. Early detection of the lung nodule is cancer for radiologists is a very challenging, time-consuming and repetitive task. The radiologist requires a great deal of time to view a number of scans with precision, while the identification of small nodules is very error-prone.

The benign and malignant nodules have a significant overlap in their characteristics [18] and must be identified at an early stage of morphology (Figure 1). Normally, benign nodules are located on the periphery with smooth surfaces and triangular forms [19] whereas malignant nodules may show limits of speculation on lobular, vascular, cystitis, pleural and sub-solid morphological boundaries [20].

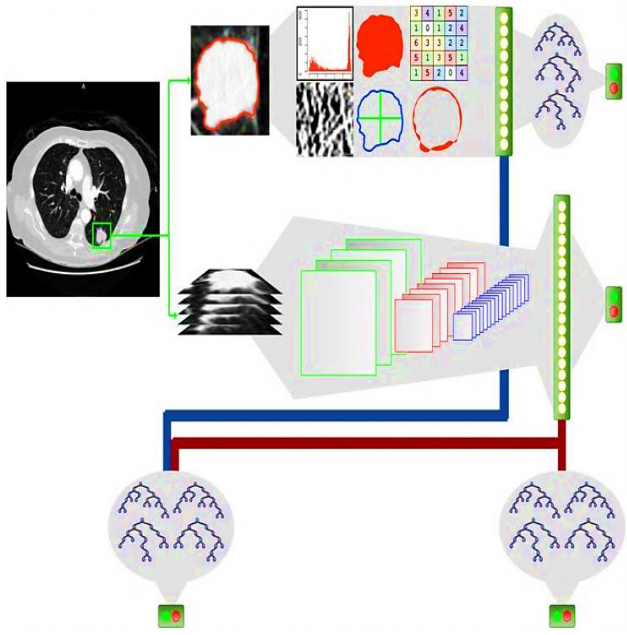

FIGURE 1. Basic Structure of Malignant lung nodules detection [21].

In addition, this study aimed to use 2D CT multi-scene images for the identification of nodules. Initially, a pitch analysis approach developed for this study resolved the distortions in lung contours induced by a juxta-pleurative nodule. Secondly, the vessel design in lung CT images has been removed with adjustable parameters. A new framework of deep learning, CNN, has been eventually developed to teach radiologists to know the two image scenes. Scene 1 consists of the original CT images, and scene 2 is made of binary images produced by complex scene 1. Throughout this way, several pairs of sub-images from an original image (Scene 1) can be compared with the binary image (Scene 2) and the sample image has been taken from https://www.ncbi.nlm.nih.gov/pmc/articles/PMC3041807/. The sub-image pairs were only images that have been captured by the CNN model This CAD system for the identification of lung nodule performs very outstanding and saves time and space for storage.

II. SURVEY ABOUT PREVIOUS WORKS

A label in a Lung CT image relates to a radiological result that suggests an abnormal disease. Analysis of CT signs helps to understand the clinical source of the lesion. A detailed study of the classification of lung nodules with various CT indications helps to make it simpler and more accurate for benign and malignant nodules. Towards this purpose, Zheng *et al.*, [22] proposed a method of classification of pulmonary nodule diagnosis based on a finish-up module with various nodular signs. Initially, they create a CNN classifier that adopts and retrains the Inception modules on Image Net. The pre-trained classification system will be completed by 10 different pulmonary sampling signals and these 10 classifiers were combined with the immune system artificial algorithm. Overall sensitivity, precision, and accuracy were proposed by Inception Network Fusion (INF) algorithms significantly higher than alternative approaches of bagging and boosting.

Rodrigues *et al.*, [23] suggested the approach of systematical co-occurrence matrix (SCM) classifying nodes as malignant nodules or benign nodules. The SCM technique was applied to eliminate nodular image characteristics and classify them as malignant or benign nodules and their malignancy. Data on nodule locations and malignancy rates are given in the computed tomography analysis of the pulmonary imaging and image database tools initiative. The SCM is implemented in four filters, in particular, medium, Laplace, Gaussian and Sobel, both grayscale and Hounsfield.

Xie *et al.*, [24] proposed to use minimum Chest CT data, a multi-visual, collaborative, and Knowledge-based (MV-KBC) model to differentiate malignant from benign nodules. This design develops the characteristics of the 3-D pulmonary nodule through the decomposition into 9 fixed views. For each view, they established a knowledge-based collaborative sub-model (KBC) where three types of image patches are built for fine-tuning three pre-trained ResNet-50 networks, each with its overall design, voxel and shape heterogeneity. The penalty loss feature is used to reduce the false-negative rate better, which minimizes the efficiency of the MV-KBC model overall. They checked and compared their system on the LIDC-IDRI standard and the 5 most advanced approaches to classification.

Chung *et al.*, [25] proposed a method of lung segmentation to reduce the problem of the juxta-pleural nodule, a popular challenge in the applications. Initially, they used Chan-Vese (CV) model for active contours and followed the Bayesian approach based on the results of a CV model that predicts lung image in an earlier frame or the neighboring image on the basis of the segmented lung contour. False positives were removed by the concave detection of points and Hough circle/ellipse was the resulting candidates. Eventually, the lung contour was changed by applying candidates from the final nodule to the results of the CV model. The high precision with the juxtapleural detection of the pulmonary nodule would support any computer-aided diagnosis system using lung segmentation as such an essential step [26]–[28].

In order to overcome the above surveys, this paper suggests an efficient identification system for lung nodules based on

Multi-Scene Deep Learning Framework (MSDLF) by the vesselness filter.

III. METHODOLOGY

A. PREPARATION OF DATA SET

The LIDC / IDRI are a public data set. A series of 1018 CT scans are gathered in this database from 1010 patients. Radiologists involved actively in the LIDC / IDRI database nodule classification. The findings of the first phase assessments are collectively implemented in the second phase by each radiologist independently. The specimens were examined again by each radiologist and the same observations were made again. Therefore, in every case of the LIDC / IDRI database, the annotations of these radiologists have an XML file. Such CT images are stored as one of the common medical standards in the DICOM format and can be checked by some image parameters for each lung CT image, with slices and pixels spacing. Once Lung CT images are obtained by various imaging devices in the LIDC / IDRI database, it normalized every pixel distance to identify 2D nodules actual dimensions. The uniform pixel length is set at 0.699 mm, which reflects the pixel length average value. Two nodules are classified as radiological records: Small nodules less than 3 mm in diameter and broad nodules greater than 3 mm in diameter. Since small nodules only have a central point label and are effectively corroded by picture filters, this conceptual model is not suitable for identifying small nodules. Consequently, the principal purpose of this analysis is to define large nodules ($>$ 3 mm) which in subsequent parts are immediately proven.

This research used 1006 scans with XML annotation files. Since data in this XML file is not easily accessible, it has created a system for data storage for annotations of the radiologist. There are a variety of detection nodules and pathological features for each radiologist (IDs). The details of such a framework are given in Figure 2. Therefore, XML files were converted to a variety of patient data structures that can be quickly extracted and coded for experiments. Furthermore, the study took level 1, which identified a nodule noted by at least 1 X-radiologist, as a real nodule to identify the true nodules for the validity of the system as golden standards.

B. MENDING OF LUNG CONTOUR AND SEGMENTATION OF PARENCHYMA

Figure. 3(a) displays a circular area consisting of machine tools, arms, spine, pulmonary lobes, fabric, etc., although a non-imaging region is located outside the circle. An automated segmentation scheme suggested by the study is implemented in four steps in order to extract the perfect lung parenchyma. The lung parenchyma segmentation process is illustrated in Figure 4.

Histogram is used in threshold segmentation to obtain the probability distribution of different gray levels. This probability distribution is determined by equation (1).

$$q(y) = \sum_{j=1}^{l} Q_j.q_j(y) = \sum_{j=1}^{l} \frac{Q_j}{\sqrt{2\pi}\rho_j} exp\left[\frac{-(y-\vartheta_j)^2}{2\rho_j^2}\right] \quad (1)$$

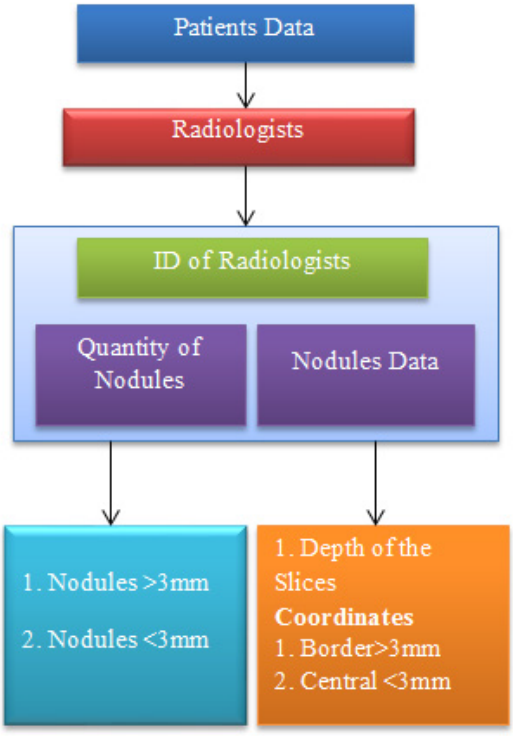

FIGURE 2. The patient's data storage system.

l represents the total number of scan image categories. Q_j and $q_j(y)$ are probability and probability distribution functions of category j. N_j is a mean and ρ_j is a standard variation. The total probability error is minimized by equation 2 for both different categories. It is used for the optimal threshold calculation.

$$e(W_j) = Q_j \int_{-\infty}^{W_j} q_j(y)\,dy + Q_{j+1} \int_{-\infty}^{W_j} Q_{j+1}(y)\,dy \quad (2)$$

This error relates to the W_j threshold and it is determined as per Equation 3.

$$E(W) = \sum_{j=1}^{l-1} e(W_j) \quad (3)$$

A threshold image is now generated with that of the lung mask.

In the first level, the luminosity and extra thoracic area in the CT images are considerably darker than chest regions. The local maximum variation between clusters thus emphasizes thoracic shape. The second step in this work is the study of the related field (4 or 8 neighborhood) and the anatomical method, along with the technique to open and close the removal of lung noise, for example, The esophagus in combination with lung type and position typical sense. A padding operator is used at the same time to fill the bubble within the lungs and to improve its contours with the area substantially below the lung lobes. The third step of this study is to establish a fast method for lung-contour mending for juxta-pleural nodules near the thorax wall that are lung

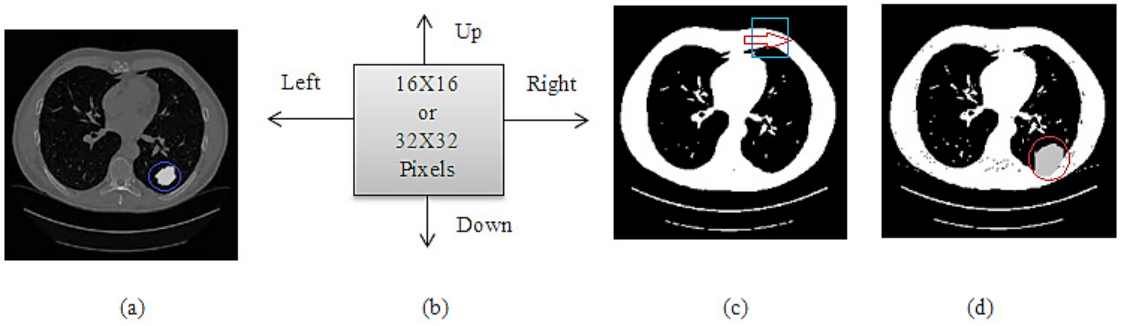

FIGURE 3. Performance of the mending and segmentation of the lung contour. (a) CT raw lung images: the circle displays the blue dotted nodes (b) two mending patch sizes (c) the lungs contour scanning process; (d) the pulmonary contours repaired.

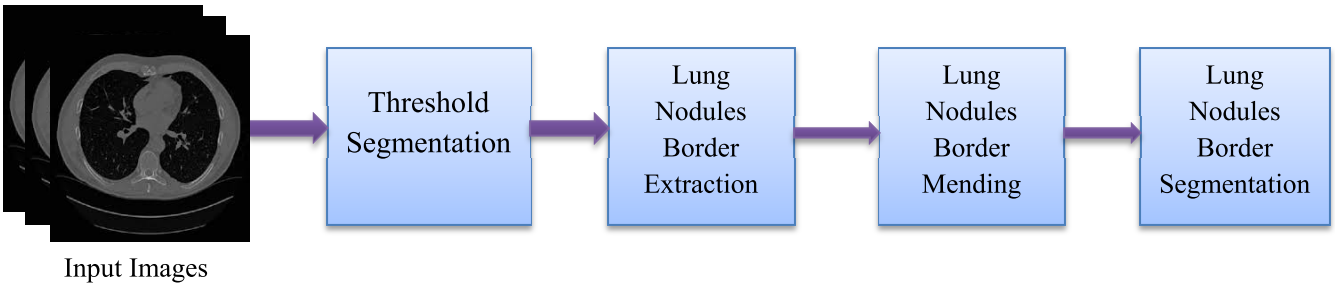

FIGURE 4. Lung parenchyma segmentation process.

tumors. Juxta-pleural nodules have been easily ignored and are considered likely to be areas outside of the lung compared with other nodule types. Regarding this issue, two sizes of patches are used for scanning the lung contour using a block of 32 × 32 pixels and a block of 16 × 16 pixels per row (Figure 3(b-d)). The main focus of this work was to correct the relatively smooth lung outline and the juxta-pleural nodules to the smooth lung outlines owing to the incidence of major cases. The change in the lung contour slope is measured using the difference method within each patch and determines whether the positions have to be addressed immediately. The boundary could be fixed automatically, depending on the position within the pulmonary, after a juxta-pleural nodule has been found. In the last step, the corrective contour of the lung parenchyma is segmented.

C. THE REMOVAL OF THE VESSEL

A large amount of tissue, polyps, veins or other contaminants is found in the lung parenchyma. Recently vascular morphology has been visible in the lung that it can affect the lung polyp identification. The images of lung CT show both cells and polyps in the similar dark pixels as luminous tissues. But the anatomy and composition of the vessels distinctly varied from the lung nodules. Tubular forms generally looked like tubes as ellipses, small circles, or cloth-like structures emerged lung nodules. The step seeks to replace the vein systems in the lung in a way that helps to examine the nodule structures. Throughout recent years, several sophisticated vessel algorithms, Different filters were suggested for Sato, Vessel Improving Diffusion (VED) and a Vessel filter. The primary use of these Vessel filters is retinal with decent performance.

One image $I(x, y)$ is shown in the field of a given point $p(x_0, y_0)$ as a Taylor series. The Taylor series's second-order concept included the Hessian matrix of $I(x, y)$, which is defined as $H_{p,\sigma}.p(x_0, y_0)$ is indicated as p, and σ is referred to as the Gaussian kernel G(x, y) size, which is expressed as Eq (5). Thus (4) and (5), as shown at the bottom of the next page, will measure $H_{p,\sigma}$. $H_{p,\sigma}$ is a matrix composed of the $I(x, y)$ and the G(x, y) derivative of the Second-order in addition to x or y.

The frequency of $H_{p,\sigma}$ and the proper vector are both measured on the σ scale, which is referred to as λ_k and $\mu_k(k = 1, 2)$. Two specific values (λ_1) and (λ_2) represent different detection mechanisms for a two-dimensional (2D) image. The path along the vessel is μ_1 and the path of orthogon μ_2 is μ_1. In discrimination against the local vascular preference, λ_1 and λ_2 plays an important role. In (6), both of the eigenvalues (λ_1) and (λ_2) indicate the vessel's calculation structure.

$$V_p = \begin{cases} 0 & if\ \lambda_2 > 0 \\ \exp\left(-|\lambda_1/\lambda_2|^2/2\beta_1^2\right) & \\ \quad (1 - \exp(\|\lambda_1, \lambda_2)\|^2/2\beta_2^2)) & otherwise \end{cases} \tag{6}$$

Therefore the β_1 and β_2 parameters are dynamic limits that can change the sensitivity of filters to $|\lambda_1/\lambda_2|$ and 2-norm$\|(\lambda_1, \lambda_2)\|$. This research was aimed at removing the vessel connections, but not at improving the vessels in lung CT images. The vessel removal method was therefore developed in two steps. Firstly, through the vesselness filter, the image of the vessel design was created under the optimum scale σ. Second, from the original pulmonary file, the image of the vessel structure produced has removed and the vessel

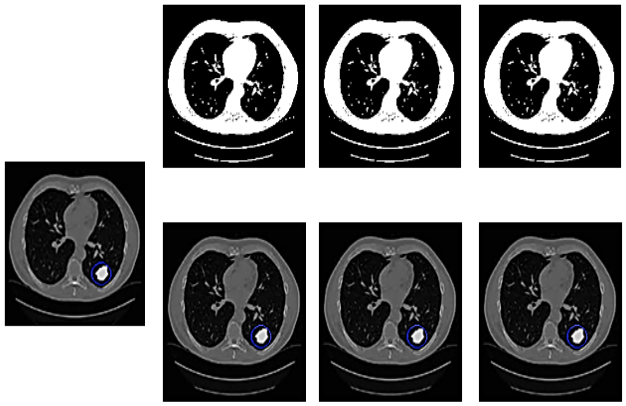

FIGURE 5. The vessel elimination compares Gaussian kernel G(x, y) to the outcome on three scales: the original image column (a-d). The result of vessel extraction in $\vartheta = 1$, 1.5 and 2. There are blue dotted circles in the nodule regions.

has deleted. The efficiency of the vessel removal of three cases is shown in Figure 5.

In vessel separation, the artery removed images are analyzed by the reference threshold system (Figure 6(a)). See that Figure 6. (c) has less suspect nodules than Figure 6.(b) so that the removal process of this vessel has the following advantages,

1. The treatment decreases the number and the nodule detection rate of the suspicious areas to be checked later.
2. It is possible to reduce the number of false positives.

D. THE DATA SET STANDARDIZATION

This paper developed a system for normalizing data in order to capture a larger data set as shown in the following Figure(7). Certainly, Nodules in images of vascular systems will easily be seen by radiologists.

In order to conserve and remove the areas of the assumed nodule lesions, both original and binary images of the vessels can be analyzed (Figure 7).

E. DESIGN OF THE CNN DESIGN

Usually, the CNN architecture comprises a convolutional layer, a pooling layer, and a fully integrated layer. The unique benefit of ReLU is that the error rate is more efficient than other activation mechanisms. It is described as

$$y_i = \max\left(0, \sum_j k_{ji} * x_j + b_i\right) \tag{7}$$

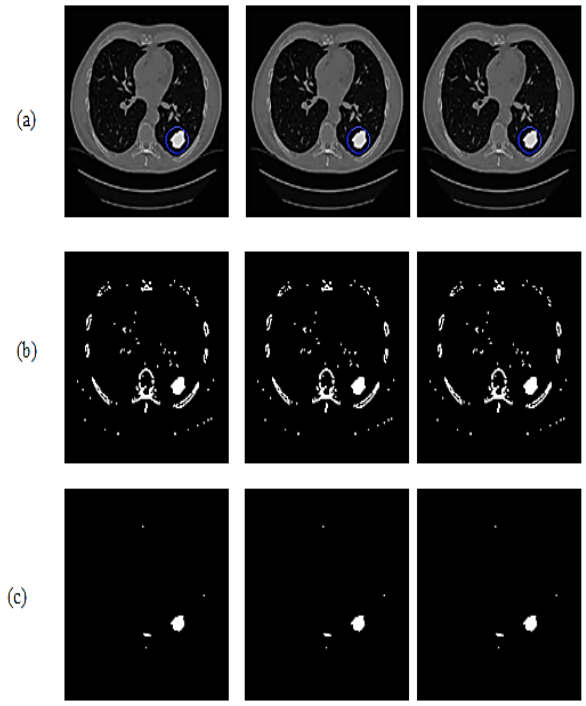

FIGURE 6. Comparison of the binarization between the representations initially portrayed by the lung and the vessel. (a) Lung image; (b) binary lung image; (c) binary lung image produced after vascular displacement from the lung image.

where the symbol x_j and b_i represent the input and output map respectively and the * symbol denotes the convolution operation. In addition, the j^{th} input map and i^{th} output map are the k_{ji} kernels. b_i is the distinctiveness of the output map i^{th}. During the training process both k_{ji} and b_i parameters can be learned. The MC pool can be shown as

$$y_i = MC_i(x), \quad i = \{0, 1\} \tag{8}$$

j^{th}-input map, i^{th}-output map, convolution kernels-k_{ji}, b_i-bias

$$MC_i(x) = \begin{cases} MP(x) & i = 0 \\ CP_i(x) & i = 1, 2, \ldots \end{cases} \tag{9}$$

where x is the map of input and y_i is the map of output. The size of x is $L \times LMP$ implies the max-pooling process and the size of $MP(x)$ is $(L/2) \times (L/2)$. CP is the center pool, meaning that the middle area of the $CP_I(x)$ is separated from x and the size of $CP_I(x)$ is $(L/2) \times (L/2)$. Similarly, $CP_i(x)$ is the central area of $CP_{i-1}(x)$ and therefore the size of $CP_2(x)$ is $(L/4) \times (L/4)$. Figure 8 will demonstrate the method of the MC pooling procedure.

$$H_{p,\sigma} = \begin{bmatrix} I(x,y) \otimes \left(\frac{\partial}{\partial x}\right)\left(\frac{\partial}{\partial x}\right) G(x,y) & I(x,y) \otimes \left(\frac{\partial}{\partial x}\right)\left(\frac{\partial}{\partial y}\right) G(x,y) \\ I(x,y) \otimes \left(\frac{\partial}{\partial x}\right)\left(\frac{\partial}{\partial y}\right) G(x,y) & I(x,y) \otimes \left(\frac{\partial}{\partial y}\right)\left(\frac{\partial}{\partial y}\right) G(x,y) \end{bmatrix} \tag{4}$$

$$G(x,y) = \left(\frac{1}{2\pi\sigma^2}\right) . \exp\left(-\|(x,y)\|^2 / 2\sigma^2\right) \tag{5}$$

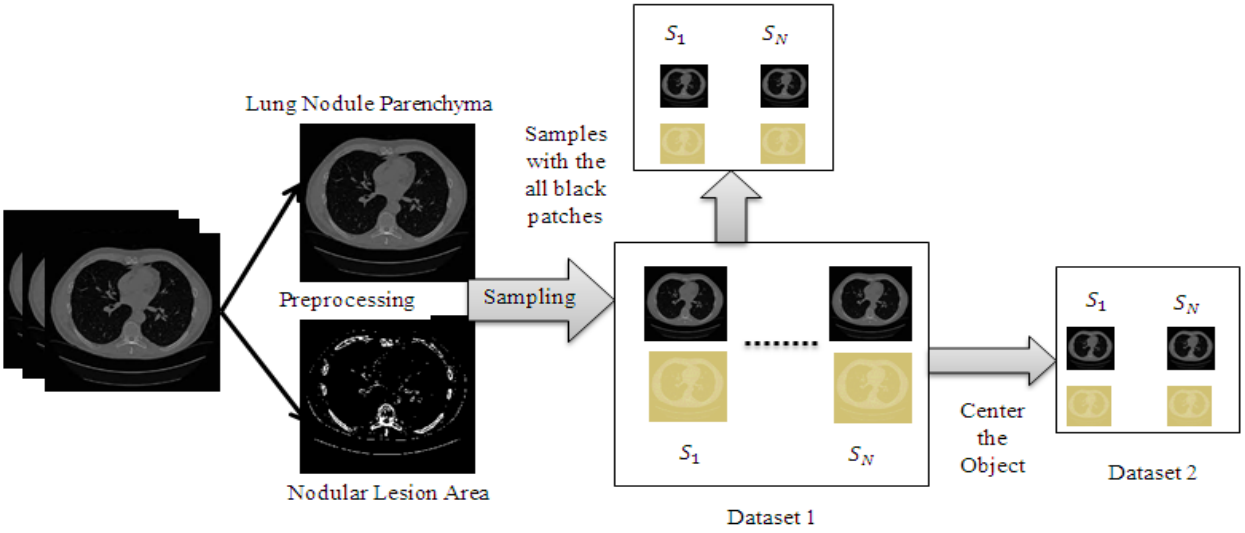

FIGURE 7. Process of normalizing nodular lesions suspected.

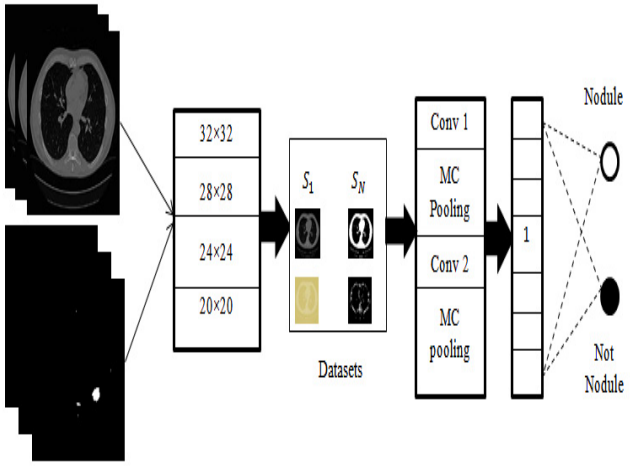

FIGURE 8. Method of MC pooling.

The role of softmax registration loss as shown by stochastic history downward gradient propagation as

$$J = -\sum_{k=1}^{C} \log\left(\frac{e^{x_k}}{\sum_{i}^{C} e^{x_i}}\right) \tag{10}$$

where x_i is the efficiency of the network, and C is the class value set to 2.

The four different patches split the nodular measurements into four different dimensions that can improve recognition precision by experimentation. Every input channel is the same location as the original image, taken from a couple of images. Further details have been demonstrated as an effective method for enhancing nodule detection.

F. SEGMENTATION AND CLASSIFICATION

Class 1 identified two classes of image data. Class 2 contained discrete images cut from the lung images removed from the vessel which has been given in figure 9. The size differences can affect detection precision, provided that the nodules varied from about 3 mm to 30 mm, which were measured by four X-rays. Every nodular stage has a patented patch identification window, a secondary image of the first pulmonary image. It helps us to split the related images and create them into classes 1 and 2. The scale of the subsidized (actual size and pixel dimension) is noted.

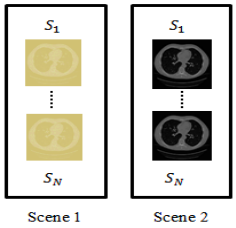

FIGURE 9. Two image data Scenes: Scene1 and 2 are the original and threshold sub-images, respectively.

Moreover, various nodule amounts are shown in Figure 10. The a, b, c modules are graded respectively in grades 1, 2, 3 and 4. The first row was the lung image processing which included radiologists identified nodule locations. The second row of threshold segmentation for the first row. Due to a small pixel gap between background and object, the threshold of OTSU had little effect on object segmentation, in the particular nodule.

This study was therefore used to look for a preferred threshold value as described in the below equation (11)

$$T = (1-\lambda).\left[\left(\sum_{i=1}^{N} P_i\right)\Big/ N\right] + \lambda.\max(P_i), \quad 1/2 \le \lambda \ge 2/3 \tag{11}$$

In (11), the P_i reflects the pixel size of the lung parenchyma. N is the cumulative lung parenchyma image and λ is a parameter customizable. When λ was between 1/2 and 2/3, the segmentation performance was beneficial. Then it Disables vibration and visual objects and retains the nodules big structures that have been described in the following

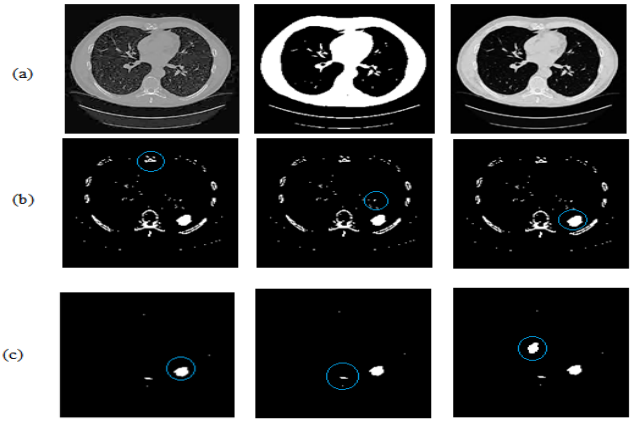

FIGURE 10. The images containing the nodule have been processed in various grades.

equation (12).

$$L(I,\sigma) = I(p) * G(p,\sigma) \tag{12}$$

where $L(I,\sigma)$ is the result of the inter-image convolution of I *and* σ and at a position p.

The second series of image I at σ scale is determined by the voxel x which is given in equation (13)

$$\frac{\partial^2 I_\sigma}{\partial x^2} = I(x) * \frac{\partial^2 G(\sigma, x)}{\partial x^2} \tag{13}$$

Since the chest CT scans contain nodules with a large variation, the response is specified across a number of σ's, with each increasing the nodules of a specific size. The final result is determined as the sum of the results from the measures under consideration. This is the cumulative response for every voxel estimated as follows:

$$V^{med}(p) = \max_{\sigma_1 \le \sigma_j \le \sigma_n} V_{\sigma_j}(p) \tag{14}$$

where j is a σ scale and n is an overall's number. The final step is a simple threshold to pick voice with high response as it receives the improved structures in which the nodules are clearly identifiable and thus establish masks by attaching the final segmentation nodule. Thresholds were collected scientifically by measuring in training sets to create a mask which would include the area inhabited by the nodule as accurately as possible. Using the greater (λ_3) and the smallest (λ_1) own values of the Hessian equation, the formula emerges from the main curve of $\sigma = 1$ as follows:

$$SI = \frac{2}{\pi} arctan\left(\frac{\lambda_3 + \lambda_1}{\lambda_3 + \lambda_1}\right) \tag{15}$$

$$CV = \sqrt{\lambda_3^2 + \lambda_1^2} \tag{16}$$

Eventually, all SI and CV thresholds are designed for the segmentation masks. The final segmentations are known to be voxels that fulfill all criteria as given below

$$V^{SI-CV} = SI \cup CV \tag{17}$$

The procedure is often observed because the chosen scale cannot be adapted to the size of the nodule, especially for large nodules. After segmentation, the characteristics must be identified accurately for the diagnosis of cancer in the lung region. The texture is used for normal and abnormal pattern recognition. The texture is an image surface modification and fluctuation.

G. NORMALIZED SPHERICAL SAMPLING

The important step in our process is a sampling. It is often known that nodule forms are not only associated with distributions of nodule size but also with anatomical structures surrounding nodules. The sampling algorithm is shown in algorithm.1.

Algorithm 1 Normalized Spherical Sampling

Input:
1: V, Volume of the nodule. r, Maximum radius of sampling.
2: $N/M/K$, Listed parameters.
Output:
3: S, Sampled dimension matrix $N \times M \times K$ for V
4: function SPHERE_SAMPLING
5: $C \leftarrow$ generate N inner centers
6: $r \leftarrow r/M$
7: $forn = 1 \rightarrow N, m = 1 \rightarrow M, k = 1 \rightarrow Kdo$
8: $r_{cur} \leftarrow r \times m$
9: $S_{nmk} \leftarrow linear\_interp(V, n, m, k)$
10: end for
11: return S
12: end function

In the above algorithm (1), the scheme is defined as the normalized spherical sample. It considers projection quality as the number of abnormal variations on the projected image, i.e. variation modifications. While all opinions are taken on their significance, another important difference is made from the features of the imaging system for a common vision and scientific image analysis. While a great deal of effort was undertaken to identify and classify lung nodules, only a few studies focused on the detection of nodule types. However, comparing methods is a necessary and reasonable step in validating our method's effectiveness. Based on the above process, the proposed work further evaluated as follows.

IV. NUMERICAL RESULTS AND DISCUSSION

Through the combination of Scene 1 and 2 referred to as Scene 1&2, we will certainly improve the performance of detection. This analysis has tested the effectiveness of Scene 1&2 and Scene 1 in demonstrating the effectiveness of Scene 1&2. Figure 11(a) to (d) shows the ROC curves after 10-fold cross-validations from the true positives (sensitivity) rating (specificity) to the false positive stage.

During this analysis, the nodules are not categorized based on their aspect in the application of the nodule detection strategy by other investigators. The analysis has shown that the separate detection of different nodular sizes (levels 1, 2, 3, 4) could be useful. The study is performed on the

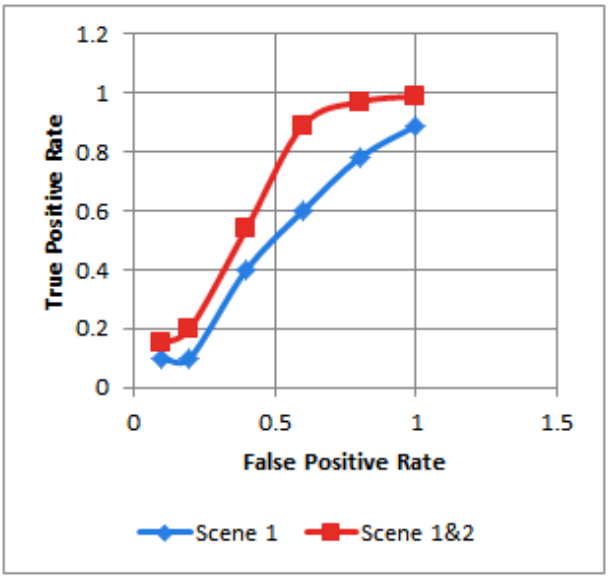

(a) Level 1

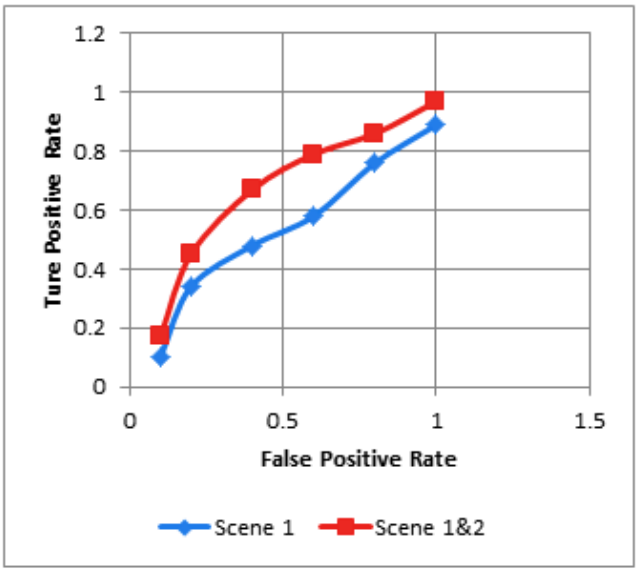

(b) Level 2

(c) Level 3

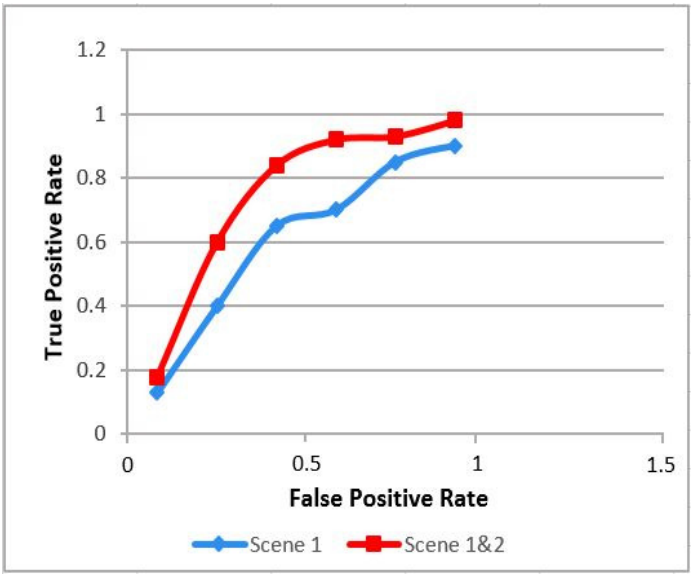

(d) Level 4

FIGURE 11. ROC curves with 4 different grade nodule rates. Red lines reflect scene 1&2 ROC curves and blue lines represent scene 1 ROC curves.

basis of existing annotations by radiologists on the sub-image distribution of 4 levels in 2D lung slices (Figure12).

However, the number of non-nodule sub-images in the scene 1&2 is approximately 300,000. It can see that smaller nodule sizes have more than large nodule sizes. Although nodules can be classified according to their status in the lung into four different types, it can only hardly help the detection of a nodule, but it can help to classify a nodule. In this experiment, two ways of detecting nodules are tried and their performance has been compared.

One strategy, like other researchers, has been to identify nodules without classification ((single level). In an additional way, four separate detections (multilevel detection) are combined under four different levels of nodules provided by this analysis. In order to determine the detection efficiency of methods, this analysis used the Free Response Receiver Characteristic (FROC). When nodules have been identified these have been verified correctly, according to the annotations of radiologists. It combines the detection results of four rates with 10-fold cross-validation. Figure 13 shows the FROC nodule detection curves under the levels 1, 2, 3, 4. Overall, the result has been the same. However, as the level increases, the less the false-positive scans show the different distributions of false-positive at the four levels of the FROC curves. It is therefore essential that it separate four different nodule levels to help throughout the identification

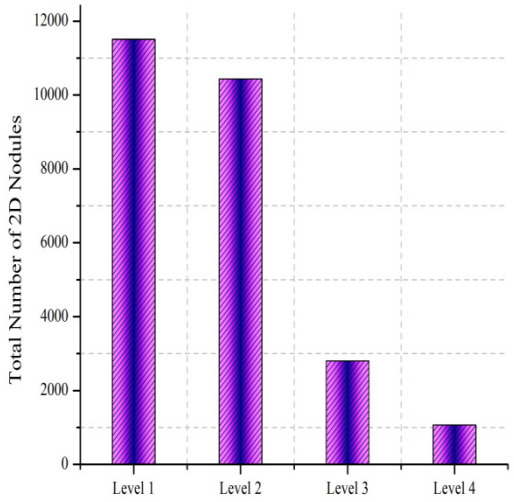

FIGURE 12. Distribution of the LIDC data set nodules of four stages.

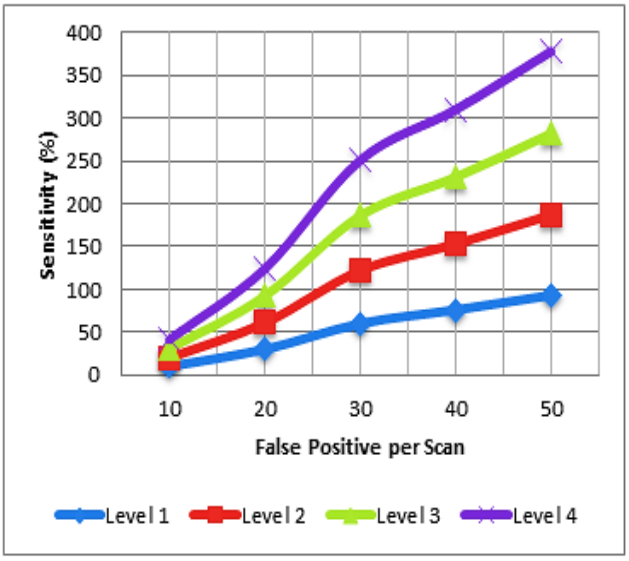

FIGURE 13. FROC four nodule rates identified.

TABLE 1. Efficiency ratio comparison.

Methods	Efficiency (%)
INF	90.4
SCM	92.6
MV-KBC	89.2
CV	90.9
MSDLF	98.7

of the nodule. In Figure 14, the final FROC curves and the unclassified Nodule detection can be shown, thus classifying nodule detection minimizing the false-positive results around the entire dataset.

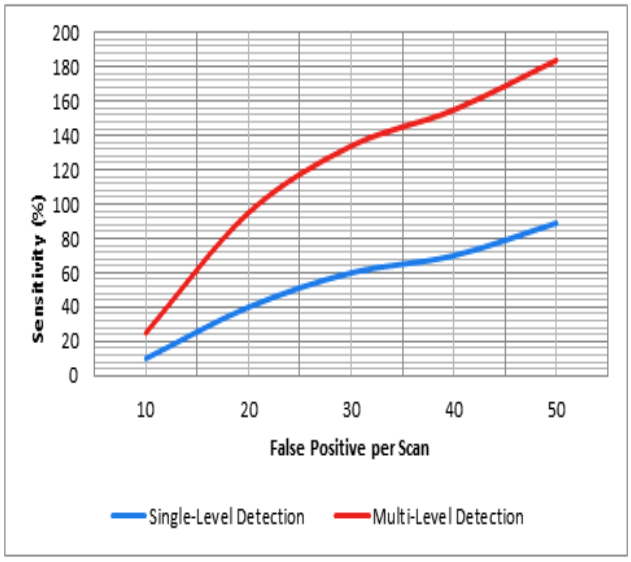

FIGURE 14. Multi-level and single-level detection of FROC curves.

As shown in Table 1, further comparative analysis is listed to demonstrate the improved efficiency of this methodology. The whole LIDC / IDRI have been used for this analysis. Thus, the lung nodules with less 3D information are abandoned. In addition, it agreed to Level 3 for the concept of a lung nodule, which means that at least 3 radiologists have to consider a lung nodule. In this study, lung nodules can be detected correctly. The proposed Multi-Scene Deep Learning Framework (MSDLF) by the vesselness filter has better efficiency when compared to other previous methods such as INF, SCM, MV-KBC, CV, MSDLF.

V. CONCLUSION

This study suggested an innovative and efficient automatic pulmonary detection system, which can reduce false positives extremely. Therefore, an automated lung wall mending mechanism is developed in this analysis to avoid missing a juxta-pleural nodule. Another significant preprocessing method in this work has been to remove the vascular disease which can illustrate nodules and weak vessels. To determine nodules accurately and quickly, four different types of CNN structures have been used and it is based on four nodule levels. In addition, the input of the CNN model is two classes of candidate nodules, containing pairs of images (Scene 1&2). Since the expertise of radiologists has been constantly increasing and improving, computer-aided systems must continue to learn from them. The automated nodule detection system for this study is used to help radiologists greatly improve detection accuracy when precious contextual relevance information from the large data is discovered.

REFERENCES

[1] E. Rendon-Gonzalez and V. Ponomaryov, "Automatic lung nodule segmentation and classification in CT images based on SVM," in *Proc. 9th Int. Kharkiv Symp. Phys. Eng. Microw., Millim. Submillim. Waves (MSMW)*, Jun. 2016, pp. 1–4.

[2] J. Tan, Y. Huo, Z. Liang, and L. Li, "Expert knowledge-infused deep learning for automatic lung nodule detection," *J. X-Ray Sci. Technol.*, vol. 27, no. 1, pp. 17–35, Apr. 2019.

[3] P. M. Shakeel, A. Tolba, Z. Al-Makhadmeh, and M. M. Jaber, "Automatic detection of lung cancer from biomedical data set using discrete AdaBoost optimized ensemble learning generalized neural networks," *Neural Comput. Appl.*, vol. 32, no. 3, pp. 777–790, Feb. 2020, doi: 10.1007/s00521-018-03972-2.

[4] X. Huang, J. Shan, and V. Vaidya, "Lung nodule detection in CT using 3D convolutional neural networks," in *Proc. IEEE 14th Int. Symp. Biomed. Imag. (ISBI)*, Apr. 2017, pp. 379–383.

[5] J.-K. Liu, H.-Y. Jiang, M.-D. Gao, C.-G. He, Y. Wang, P. Wang, H. Ma, and Y. Li, "An assisted diagnosis system for detection of early pulmonary nodule in computed tomography images," *J. Med. Syst.*, vol. 41, no. 2, p. 30, Feb. 2017.

[6] P. M. Shakeel, M. I. Desa, and M. A. Burhanuddin, "Improved watershed histogram thresholding with probabilistic neural networks for lung cancer diagnosis for CBMIR systems," *Multimedia Tools Appl.*, vol. 78, 2019.

[7] E. Soleymanpour, H. Pourreza, E. Ansaripour, and M. Yazdi, "Fully automatic lung segmentation and rib suppression methods to improve nodule detection in chest radiographs," *J. Med. Signals Sensors*, vol. 1, no. 3, p. 6, 2011.

[8] N. Khosravan and U. Bagci, "S4ND: Single-shot single-scale lung nodule detection," in *Proc. Int. Conf. Med. Image Comput. Comput.-Assist. Intervent.*, Cham, Switzerland: Springer, Sep. 2018, pp. 794–802.

[9] Y. Gu, X. Lu, L. Yang, B. Zhang, D. Yu, Y. Zhao, L. Gao, L. Wu, and T. Zhou, "Automatic lung nodule detection using a 3D deep convolutional neural network combined with a multi-scale prediction strategy in chest CTs," *Comput. Biol. Med.*, vol. 103, pp. 220–231, Dec. 2018.

[10] A. Teramoto and H. Fujita, "Fast lung nodule detection in chest CT images using cylindrical nodule-enhancement filter," *Int. J. Comput. Assist. Radiol. Surg.*, vol. 8, no. 2, pp. 193–205, Mar. 2013.

[11] P. M. Shakeel, M. A. Burhanuddin, and M. I. Desa, "Lung cancer detection from CT image using improved profuse clustering and deep learning instantaneously trained neural networks," *Measurement*, vol. 145, pp. 702–712, Oct. 2019, doi: 10.1016/j.measurement.2019.05.027.

[12] W. Li, P. Cao, D. Zhao, and J. Wang, "Pulmonary nodule classification with deep convolutional neural networks on computed tomography images," *Comput. Math. Methods Med.*, vol. 2016, pp. 1–7, Dec. 2016.

[13] M. Saii and A. Mayya, "Lung detection and segmentation using marker watershed and Laplacian filtering," *Int. J. Biomed. Eng. Clin. Sci.*, vol. 1, no. 2, pp. 29–42, 2015.

[14] S. L. A. Lee, A. Z. Kouzani, and E. J. Hu, "Automated detection of lung nodules in computed tomography images: A review," *Mach. Vis. Appl.*, vol. 23, no. 1, pp. 151–163, Jan. 2012.

[15] E. Dandıl,"A computer-aided pipeline for automatic lung cancer classification on computed tomography scans," *J. Healthcare Eng.*, vol. 2018, pp. 1–12, Nov. 2018.

[16] W. Zhu, C. Liu, W. Fan, and X. Xie, "DeepLung: Deep 3D dual path nets for automated pulmonary nodule detection and classification," in *Proc. IEEE Winter Conf. Appl. Comput. Vis. (WACV)*, Mar. 2018, pp. 673–681.

[17] Y. Zhao, L. Zhao, Z. Yan, M. Wolf, and Y. Zhan, "A deep-learning based automatic pulmonary nodule detection system," *Proc. SPIE*, vol. 10575, Feb. 2018, Art. no. 1057537.

[18] E. Dandil, M. Cakiroglu, Z. Eksi, M. Ozkan, O. K. Kurt, and A. Canan, "Artificial neural network-based classification system for lung nodules on computed tomography scans," in *Proc. 6th Int. Conf. Soft Comput. Pattern Recognit. (SoCPaR)*, Aug. 2014, pp. 382–386.

[19] A. A. A. Setio, C. Jacobs, J. Gelderblom, and B. van Ginneken, "Automatic detection of large pulmonary solid nodules in thoracic CT images," *Med. Phys.*, vol. 42, no. 10, pp. 5642–5653, Sep. 2015.

[20] S. Akram, M. Y. Javed, M. U. Akram, U. Qamar, and A. Hassan, "Pulmonary nodules detection and classification using hybrid features from computerized tomographic images," *J. Med. Imag. Health Informat.*, vol. 6, no. 1, pp. 252–259, Feb. 2016.

[21] J. L. Causey, J. Zhang, S. Ma, B. Jiang, J. A. Qualls, D. G. Politte, F. Prior, S. Zhang, and X. Huang, "Highly accurate model for prediction of lung nodule malignancy with CT scans," *Sci. Rep.*, vol. 8, no. 1, pp. 1–12, Dec. 2018.

[22] G. Zheng, G. Han, and N. Q. Soomro, "An inception module CNN classifiers fusion method on pulmonary nodule diagnosis by signs," *Tsinghua Sci. Technol.*, vol. 25, no. 3, pp. 368–383, Jun. 2020.

[23] M. B. Rodrigues, R. V. M. Da Nobrega, S. S. A. Alves, P. P. R. Filho, J. B. F. Duarte, A. K. Sangaiah, and V. H. C. De Albuquerque, "Health of things algorithms for malignancy level classification of lung nodules," *IEEE Access*, vol. 6, pp. 18592–18601, 2018.

[24] Y. Xie, Y. Xia, J. Zhang, Y. Song, D. Feng, M. Fulham, and W. Cai, "Knowledge-based collaborative deep learning for benign-malignant lung nodule classification on chest CT," *IEEE Trans. Med. Imag.*, vol. 38, no. 4, pp. 991–1004, Apr. 2019.

[25] H. Chung, H. Ko, S. J. Jeon, K.-H. Yoon, and J. Lee, "Automatic lung segmentation with juxta-pleural nodule identification using active contour model and Bayesian approach," *IEEE J. Translational Eng. Health Med.*, vol. 6, 2018, Art. no. 1800513.

[26] W. Li, M. Jia, J. Wang, J. Lu, J. Deng, J. Tang, and C. Liu, "Association of MMP9-1562C/T and MMP13-77A/G polymorphisms with non-small cell lung cancer in southern chinese population," *Biomolecules*, vol. 9, no. 3, p. 107, 2019.

[27] Y. Lou, J. Yang, L. Wang, X. Chen, X. Xin, and Y. Liu, "The clinical efficacy study of treatment to chiari malformation type i with syringomyelia under the minimally invasive surgery of resection of submeningeal cerebellar tonsillar herniation and reconstruction of cisterna magna," *Saudi J. Biol. Sci.*, vol. 26, no. 8, pp. 1927–1931, Dec. 2019.

[28] Y. Ren, X. Jiao, and L. Zhang, "Expression level of fibroblast growth factor 5 (FGF5) in the peripheral blood of primary hypertension and its clinical significance," *Saudi J. Biol. Sci.*, vol. 25, no. 3, pp. 469–473, Mar. 2018.

QINGHAI ZHANG was born in 1965. He received the degree. He is currently a Deputy Chief Physician. In 1986, he joined in imaging diagnosis, for more than 30 years. He successively went to the Jinan Military Region General Hospital, Shandong Provincial Institute of Imaging, and 301 Hospital to study CT / MR diagnostics and CT interventional therapy. In practical work, he is also good at learning and summarizing, is diligent in studying and thinking, dares to challenge traditional theories with innovative thinking, and has accumulated rich clinical and practical experience. On the basis of fully mastering common and frequently-occurring imaging diagnosis, in obstetric diseases, we have our own unique insights. He has authored more than ten national academic articles, including four national core journals and two scientific research achievements.

XIAOJING KONG was born in 1979. He received the degree from college. He has participated in 2003, involved in imaging diagnosis, for more than 17 years, and successively studied at the PLA General Hospital, Tianjin Cancer Hospital, Shandong Institute of Imaging. He has accumulated a lot of practice and experience in imaging diagnosis, especially in obstetrics and gynecology, pediatrics, and breast diseases. He has unique insights and rich experience. He is currently an Attending Physician. He has published two core journal articles, two national articles, and one scientific research achievement.